OPTICA

Scalable low-latency optical phase sensor array

Zhanghao Sun,[1,*] Sunil Pai,[1] Carson Valdez,[1] Maziyar Milanizadeh,[2] Andrea Melloni,[2] Francesco Morichetti,[2] David A. B. Miller,[1] and Olav Solgaard[1]

[1]Ginzton Laboratory, Stanford University, 348 Via Pueblo Mall, Stanford, California 94305, USA
[2]Department of Electronics, Information and Bioengineering, Politecnico di Milano, via Ponzio 34/5, 20133, Milano, Italy
*zhsun@stanford.edu

Optical phase measurement is critical for many applications, and traditional approaches often suffer from mechanical instability, temporal latency, and computational complexity. In this paper, we describe compact phase sensor arrays based on integrated photonics, which enable accurate and scalable reference-free phase sensing in a few measurement steps. This is achieved by connecting multiple two-port phase sensors into a graph to measure relative phases between neighboring and distant spatial locations. We propose an efficient post-processing algorithm, as well as circuit design rules to reduce random and biased error accumulations. We demonstrate the effectiveness of our system in both simulations and experiments with photonics integrated circuits. The proposed system measures the optical phase directly without the need for external references or spatial light modulators, thus providing significant benefits for applications including microscope imaging and optical phased arrays. © 2023 Optica Publishing Group under the terms of the Optica Open Access Publishing Agreement

1. INTRODUCTION

Optical phase measurements are important in imaging [1–5], environmental sensing [6,7], optical communications [8–11], and optical neural networks [12–15]. Previous approaches for optical phase measurement can be divided into two categories: reference based and reference free. The first approach is based on homodyne/heterodyne interference between the detected optical field and a reference signal directly routed from the light source [16,17]. Such systems benefit from the improved detection signal-to-noise ratio (SNR) while suffering from any instabilities in the reference arm [17–20]. The reference-free approach avoids the need for an external reference by interfering different components of the incident field with one another [21–23]. Phase contrast microscopy exploits a phase shifting aperture to interfere the incident light field with a plane wave and acquires an approximate phase profile for transparent samples [1]. Modern reference-free wavefront measurements typically use a programmable spatial light modulator (SLM) together with post-processing with phase retrieval algorithms that lead to significant computational cost [23–25]. In a special case, the Shack–Hartmann (SH) wavefront sensor [26] employs a micro-lens array instead of an SLM.

Recently, a reference-free optical field measurement based on a photonics integrated circuit (PIC) has been proposed and demonstrated [27,28]. During operation, Mach–Zehnder interferometers (MZIs) in the PIC are *progressively* configured through power minimizations, and the relative input optical phase over all the inputs is calculated based on the phase settings. This approach is robust against vibrations [29], but it requires that the MZIs are

controlled by analog voltages of high precision, and its progressive nature of successive minimizations introduces significant time delay.

In this paper, we propose a compact photonics phase sensor array for reference-free phase sensing requiring only a few measurements. This is achieved by connecting multiple two-port phase sensors (Section 2) into a graph to measure relative phases (phase gradients) between both neighboring and *distant* spatial locations. Due to the versatile PIC platform, all measurements are conducted in parallel in a single photonics focal-plane [3]. Compared to the progressive PIC phase measurement, our system has lower latency and requires less hardware.

To minimize measurement errors caused by sensor noise, we add post-processing, formulated as a least squares problem. Compared with non-convex phase retrieval algorithms, the post-processing in our system is fast and robust (Section 3).

We analyze the phase sensor array's robustness to noise and hardware errors for large numbers of input ports (Sections 4 and 5). Phase sensing accuracy is shown to be determined by the connectivity of the photonics circuit. Errors can be significantly reduced by (1) introducing distant relative phase measurements, (2) appropriately placing phase shifters in phase sensors, and (3) introducing redundant relative phase measurements. We demonstrate the effectiveness of our designs both with simulations and through experiments. The proposed system is promising in various applications, including phase imaging in microscopy and in optical phased arrays (OPAs) [30]; we simulate two example applications in Section 6. In Section 7, we systematically compare the proposed

phase sensor array to the progressive approach [27] in various metrics, including scalability, speed, and complexity.

2. INTEGRATED PHASE SENSOR

We start with the description of a single two-port phase sensor, which detects the relative phases between two input optical fields x_1, x_2 that enter the phase sensor in single mode waveguides. Similar devices have recently been applied in reference-based detection systems [3,29]. As shown in Fig. 1(a), a straightforward implementation uses in-phase and quadrature (I/Q) interferometric detection [29] with a 50/50 beam splitter and a tunable phase shifter. The system can be modeled as a 2-in, 2-out linear system with transmission matrix H:

$$H = B R(\zeta) = \frac{1}{\sqrt{2}} \begin{bmatrix} 1 & i \\ i & 1 \end{bmatrix} \begin{bmatrix} e^{i\zeta} & 0 \\ 0 & 1 \end{bmatrix}. \quad (1)$$

Here B, R are the transmission matrices of the 50/50 beam splitter and phase shifter, respectively. When the phase shift ζ is set to zero (b_+ and b_- outputs) and $\pi/2$ (h_+ and h_-), the detected optical powers in the two photodetectors are

$$h_\pm = (|x_1|^2 + |x_2|^2 \pm 2|x_1||x_2|\cos\gamma)/2,$$

$$b_\pm = (|x_1|^2 + |x_2|^2 \pm 2|x_1||x_2|\sin\gamma)/2, \quad (2)$$

where γ is the relative phase between x_1, x_2. Equation (2) gives the estimate $\gamma = \arctan((b_+ - b_-)/(h_+ - h_-))$. This active sensor design requires two measurement steps and utilizes one phase shifter whose phase delay is switched between zero and $\pi/2$. To avoid the delay of actively tuning the phase shifter, we use the passive sensor shown in Fig. 1(b), in which $h_\pm$ and $b_\pm$ are measured in one step, although the optical power in each photodetector is reduced. (In the following, we assume all directional couplers in the circuit are 50/50 beam splitters unless mentioned, while the two on the sides can be designed to have beam splitting ratios other than 50/50.)

To simplify the following discussions and visualizations, we abstract the phase sensor into a graph without the physical implementation details [31]. As shown in Fig. 1(c), each input port is represented by a vertex in the graph, and each phase sensor is represented by an edge. Since the phase shifter is applied to only one arm in the sensor, the phase sensor, and hence the edge that represents
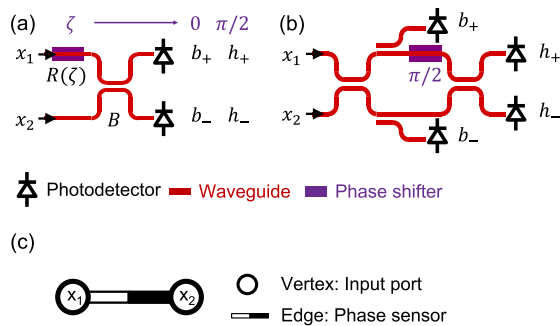
it, is asymmetrical, and we define the input port on the side with the phase shifter or on the side with the $\pi/2$ phase shift path to have positive polarity (the white end of the white–black edge). While a more standard concept in graph theory is a directed edge, we use polarity to represent this asymmetry to avoid confusion with the optical power propagation direction.

3. PHASE SENSOR ARRAY

Multiple phase sensors can be integrated into an array to measure the phase profile across multiple input ports, as shown in Fig. 2(a). When the system is used to measure a free-space light field, an optical interface converts free-space incident light to the phase sensor using grating couplers (GCs), photonics lantern, or other free-space optical interface [32–34] (please refer to Supplement 1 for a polarization sensitive interface). At each input port of the sensor, the received optical signal is split into multiple single-mode waveguides [35] and then fed into the phase sensors, as shown by the black arrows in Fig. 2(a). Following the conventions defined in Section 2, we also show the corresponding graph representation in Fig. 2(b). Each phase sensor is accessed independently, and the input light is routed to the photodetectors and converted into electronic signals. The electronic readout circuitry can be similar to that of common image sensors [36].

From the readout of photodetectors, the phase measurement of each phase sensor is calculated using Eq. (2). For the example shown in Fig. 2, the sensor array has four input ports $\{x_1, x_2, x_3, x_4\}$ (without loss of generality, we select x_1 to be zero phase). We need to find three unknown phase differences relative to the phase of x_1, $\mathbf{p} = \{p_2, p_3, p_4\}$, and there are four phase sensors $\{H_1, H_2, H_3, H_4\}$ in the array with measurement results $\mathbf{p}_H = \{p_{H_1}, p_{H_2}, p_{H_3}, p_{H_4}\}$. The measurement process can be expressed in a matrix M:

$$\begin{matrix} \mathbf{p}_H & M & \mathbf{p} & \mathbf{e}_H \\ \begin{bmatrix} p_{H_1} \\ p_{H_2} \\ p_{H_3} \\ p_{H_4} \end{bmatrix} = \begin{bmatrix} 1 & -1 & 0 & 0 \\ 0 & 1 & -1 & 0 \\ 0 & 0 & 1 & -1 \\ -1 & 0 & 0 & 1 \end{bmatrix} & \begin{bmatrix} 0 \\ p_2 \\ p_3 \\ p_4 \end{bmatrix} + \begin{bmatrix} e_{H_1} \\ e_{H_2} \\ e_{H_3} \\ e_{H_4} \end{bmatrix}, \end{matrix} \quad (3)$$

where $\mathbf{e}_H = \{e_{H_i}\}$ are the phase measurement errors. When the number of phase sensors is one less than the number of input ports
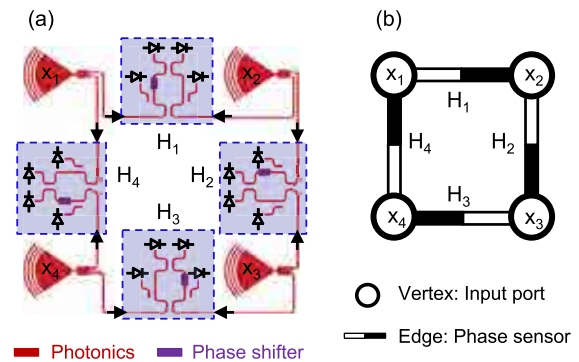

Fig. 1. (a) Active phase sensor using a phase shifter followed by a beam splitter. (b) Passive phase sensor. (c) Graph representation of a single phase sensor. The vertex (circle) represents an input port, while the edge represents a phase sensor. The polarity of the edge represents the placement of the phase shifter in the sensor. Formally, the white end of the edge in (c) corresponds to the port or side of the phase sensor that has the phase shifter, as in (a), or the $\pi/2$ phase shift, as in (b).

Fig. 2. (a) Simple example of phase sensor array with four input ports and four phase sensors (not to scale) and (b) corresponding graph representation. Black arrows in (a) show the optical power propagation directions, and black/white colored edges in (b) represent the phase sensors with polarities. To handle the measurement errors, a least squares method is used to compute the phase profile from phase sensor measurements.

(we call it a "non-redundant" array in Section 5.A), **p** can be recovered from $\mathbf{p}_H$ by algebraic calculations. However, in more general cases (e.g., Fig. 2), the number of phase measurements exceeds the number of unknown phases. In those cases, we solve a least squares problem to better account for measurement errors, with the pseudo-inverse of the measurement matrix $M^+ = (M^T M)^{-1} M^T$ [37]:

$$
\begin{cases}
\hat{\boldsymbol{p}} = \arg\min_{\mathbf{p}} |\mathbf{p}_H - M\mathbf{p}|^2 = M^+ \mathbf{p}_H, \\
\mathbf{p} = (0, \, p_2, \, p_3, \, p_4)^T, \\
\mathbf{p}_H = (p_{H_1}, \, p_{H_2}, \, p_{H_3}, \, p_{H_4})^T,
\end{cases}
\tag{4}
$$

where $\hat{\boldsymbol{p}}$ is the estimated phase profile. In our system, each row in M corresponds to the measurement made by one phase sensor. The measurement matrix has a $+1$ element and -1 element in each row, with all other elements zero. Switching the position of the phase shifter from one arm to the other arm in the phase sensor results in a change of sign in the corresponding row in matrix M. Since matrix M is determined once the device is fabricated, so is the pseudo-inverse M^+ (which can be deduced from the singular value decomposition of M). Solving this least squares problem then requires only a simple matrix–vector multiplication between M^+ and the vector of measurements $\mathbf{p}_H$.

Note that due to the 2π ambiguity of phase, the first line of Eq. (4) should be expressed as $\hat{\boldsymbol{p}} = \arg\min_{\mathbf{p}} |\mathrm{mod}[(\mathbf{p}_H - M\mathbf{p}), 2\pi]|^2$, where $\mathrm{mod}[\,, 2\pi]$ is the modulo operation. This is different from a normal least squares problem. However, a simple workaround converts it into a normal least squares problem (please refer to Supplement 1 for more details). Therefore, we still use the normal least squares optimization formula for simplicity.

4. PHASE SENSING ERROR

There are two major sources of error in the phase measurements. The first is noise in photodetection, including photon shot noise [38,39], dark current [40], and amplifier readout noise [41]. The second source is systematic hardware errors, including incorrect beam splitting ratios and phase shifts [42,43], and non-uniform photodetector gain [20]. Such systematic errors can be partially removed by calibration (similar to that in free-space interferometers [19,20]; detailed calibration process is described in Supplement 1). Typical residual errors in the beam splitting ratio reported in the literature are ~1% to 10% [12,42]. Note that hardware errors can be random or biased. Random hardware error means every single element in the system has different imperfections [44,45], while biased hardware error means all elements in the system are biased to the same erroneous state. Such biased error can be due to temperature, optical wavelength, fabrication, or other global factors. In the following, we discuss only beam splitting errors, while all the conclusions can be straightforwardly applied to other types of hardware errors (e.g., phase shifter error). Please refer to Supplement 1 for details.

We use simulations to evaluate the influence of noise and hardware errors on phase sensing accuracy. We first consider a single phase sensor. Under specific noise and hardware errors, we use the expectation of absolute error of measured relative phase $\mathbb{E}[\mathrm{RMS}] = \mathbb{E}[||\hat{p} - p||]$ to characterize the average phase sensing error. Following the convention in [42], the expectation is taken over a set of random input fields:
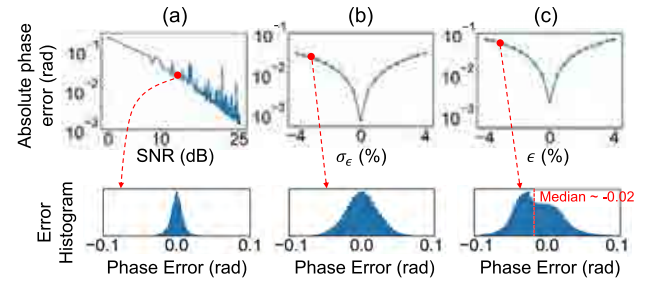

Fig. 3. Single sensor phase measurement error (absolute values averaged over 1000 random input fields simulations) with (a) photodetection noise, (b) random beam splitter error, and (c) biased beam splitter error. Second row: corresponding measurement error histograms at the red dot indicated settings (over 1000 random input field simulations).

$$
x \sim (\mathcal{N}(0, 1) + i\mathcal{N}(0, 1))/\sqrt{2}, \quad \mathbb{E}[|x|^2] = 1,
$$

$$
h'_{\pm} = h_{\pm} + \sigma_n \mathcal{N}(0, 1), \quad b'_{\pm} = b_{\pm} + \sigma_n \mathcal{N}(0, 1),
$$

$$
\mathrm{SNR} := \mathbb{E}[|x|^2]/\sigma_n = 1/\sigma_n,
\tag{5}
$$

where $\mathcal{N}(0, 1)$ is the normal distribution with mean zero and standard deviation one, $h'_{\pm}$ and $b'_{\pm}$ are noisy measurements, and σ_n is the magnitude of measurement noise. For simplicity, we use a simple noise model and define the overall SNR of the system as $1/\sigma_n$. For hardware errors, we simulate random and biased beam splitter errors (BSE). Similar to Eq. (1), the imperfect beam splitter with an uneven splitting ratio is modeled by the 2×2 matrix $B' = \frac{1}{\sqrt{2}} \begin{bmatrix} \sqrt{1+\epsilon} & i\sqrt{1-\epsilon} \\ i\sqrt{1-\epsilon} & \sqrt{1+\epsilon} \end{bmatrix}$, where ϵ is the error. For the random error case, we assume $\epsilon \sim \sigma_\epsilon \mathcal{N}(0, 1)$. For the biased error case, we use the same ϵ for all beam splitters. For all hardware error simulations, we still include photodetection noise.

The simulated average phase sensing errors in Figs. 3(a)–3(c) show several important results. First, except under extremely low SNR, average phase sensing error is inversely proportional to the SNR when no hardware error is present. Second, hardware errors significantly increase phase sensing errors. Third, biased hardware errors cause biased phase sensing error [as shown in Fig. 3(c), with median ~−0.02].

5. PHASE SENSING ERROR IN ARRAY

We denote the phase sensing error at phase sensor i as e_{Hi}. Following the simulation results in Fig. 3, we can decompose the statistical distributions of phase sensing error into a standard deviation σ_e and a bias e_0. Since the phase profile in a sensor array is estimated by Eq. (4), we characterize the average *estimated* phase sensing accuracy with the expected root mean square error (RMSE) $\mathbb{E}[\mathrm{RMS}] = \mathbb{E}[||\hat{\boldsymbol{p}} - \mathbf{p}||]$. Similar to Section 4, the expected value is taken over random input fields following Eq. (5).

Figure 4, left side ("1D chain" configuration), shows an example of the phase sensor array. The expectation of phase RMSE for a phase sensor array with N input ports can be expressed as
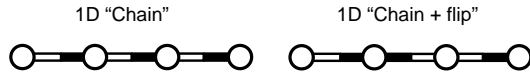
Fig. 4. Left: "1D chain" configuration. Right: "1D chain + flip" configuration. While random error accumulation remains the same, biased error accumulation is eliminated.

$$\mathbb{E}[(\hat{p}_i - p_i)^2] = \sum_{j=1}^{i} \mathbb{E}[e_{Hi}^2] = i\sigma_e^2 + i^2 e_0^2,$$

$$
\begin{aligned}
\mathbb{E}[\text{RMS}] &= \sqrt{\mathbb{E}\left[\frac{1}{N}\sum_{i=1}^{N-1}(\hat{p}_i - p_i)^2\right]} \\
&= \sqrt{\sigma_e^2(N-1)/2 + e_0^2(N+1)(2N+1)/6} \\
&= \sqrt{\text{E}_r^2 + \text{E}_b^2}. \quad (6)
\end{aligned}
$$

We can divide $\mathbb{E}[\text{RMS}]$ into contributions from the random error in each sensor σ_e [E_r, scales with $O(\sqrt{N})$] and the bias error e_0 [E_b, scales with $O(N)$]. This error becomes intolerable with moderate N thus prohibiting scaling up.

Equation (6) also indicates that the expected error at the ith port $\{\mathbb{E}[(\hat{p}_i - p_i)^2]\}$ depends on the number of intermediate connections (path length in graph theory) between it and the reference port, as shown in Fig. 4. The shorter the path length, the fewer accumulated errors. The key difference between random and biased errors lies in their dependencies on the polarities of the phase sensors. E_r does not change when the polarities of the connections change, while E_b largely depends on the polarities. By flipping the edge (phase sensor) polarities in the 1D chain configuration, $\text{E}_b = e_0$ (constant w.r.t N) is achieved in the "1D chain + flip" configuration (Fig. 4 right side).

For more complex circuit configurations, analytical relationships between N and E_r, E_b are difficult to obtain. Nonetheless, following Eq. (4), we can establish a simple relationship between the RMSE and M^+, the pseudo-inverse of measurement matrix M (derivations are presented in Supplement 1):

$$
\begin{cases}
\text{E}_r = \sigma_e \sqrt{\sum_{ij} M^+[ij]^2}, \\
\text{E}_b = e_0 \sqrt{\sum_{ij} (M^{+T}M^+)[ij]},
\end{cases} \quad (7)
$$

$$M^+ = (M^T M)^{-1} M^T.$$

Note that $\sqrt{\sum_{ij} M^+[ij]^2}$ and $\sqrt{\sum_{ij}(M^{+T}M^+)[ij]}$ are the Frobenius and $L_{2,1}$ norms of matrix M^+, respectively, and are related to "graph spectrum" in graph theory [46]. From Eq. (7), we again observe that flipping signs of the rows in matrix M will not change E_r, but has an influence on E_b. Therefore, these two metrics are decoupled and can be considered separately in the circuit configuration design: we first ignore the polarities in the circuit graph and minimize E_r by placing edges (phase sensors) at proper positions. In particular, we want to minimize the path lengths from the reference port to other ports in the circuit graph. Then we flip the polarities for part of the edges to minimize E_b. Due to this decoupled design rule, in the following, we ignore the phase sensor polarity when discussing E_r, and we always assume

that there exists a phase sensor polarity arrangement to minimize E_b.

A. Non-redundant Array

The minimum number of phase sensors needed to measure a full phase profile with N input ports is $N - 1$. We denote this type of circuits as non-redundant. Several examples are shown in Fig. 5(a) (polarities of phase sensors are ignored, as discussed above). Since only one path exists between the phase reference input to any other input, the design rule of "shorter path, lower error" holds. The most naive chain configuration has $\text{E}_r \sim O(\sqrt{N})$, which becomes intolerable with moderate N. By breaking the long path into shorter ones, E_r is reduced to $O(N^{1/4})$ in a "split chain" configuration. With $N = 1000$, this is $\sim 6 \times$ smaller than the simple 1D chain configuration of Fig. 4. Similar configurations can also be implemented with input ports arranged in 2D. Through bi-sectioning the long path, the "bi-section" configuration achieves $O(\sqrt{\log N})$ RMSE. However, this configuration requires complicated waveguide routings that increase the footprint significantly. In all these configurations, E_b can be reduced to $O(1)$ (constant) by flipping the polarities of edges.

We simulate the average phase sensing accuracy with photodetection noise [Fig. 5(b)] SNR $= 30$ dB. The simulation results fit well with the theoretical analysis.

B. Redundant Array

Redundant phase sensing elements can be introduced into the circuit as shown in Fig. 5(a). In the redundant array, multiple paths exist between the phase reference input and other unknown phase inputs, so the least squares optimization is effectively performing an averaging over phase estimation results accumulated along all paths. With more redundancies, more paths are involved in the averaging and thus provide a more accurate estimate. On the other hand, with more redundancies, each input port is connected to more phase sensors, and each phase sensor is receiving less optical power, resulting in lower SNR.

We show two representative cases in Fig. 5(b). In the best case, $O(\log N)$ is achieved in the grid configuration with flipped edges. The "grid + diag" configuration has 50% more edges (phase sensors) compared to the grid configuration. However, the phase sensing accuracies are similar, due to the trade-off discussed above. We also show an example with biased BSEs [Fig. 5(c)]. Similar to single phase sensor simulations, we use biased BSE $= 1\%, 4\%$ in this simulation. It can be seen that with correctly flipped edges, phase sensing error maintains $O(\log N)$ scalability, while failing to do so results in phase sensing error $\sim O(\sqrt{N})$.

C. Experimental Results

We demonstrate the effectiveness of redundant phase sensor arrays on a fabricated silicon PIC platform [a single active phase sensor is shown in Fig. 6(a)] [12]. We use a reconfigurable photonics circuit to detect optical power, and emulate different connection configurations between phase sensors (refer to Supplement 1 for detailed hardware implementation). We use tap GCs as an alternative for integrated photodetectors, following the design in [12]. The tap GC couples out 3% optical power from the waveguide and emits to an IR camera sitting on top of the device. Our circuit consists of five input ports, and the non-redundant configuration consists of four
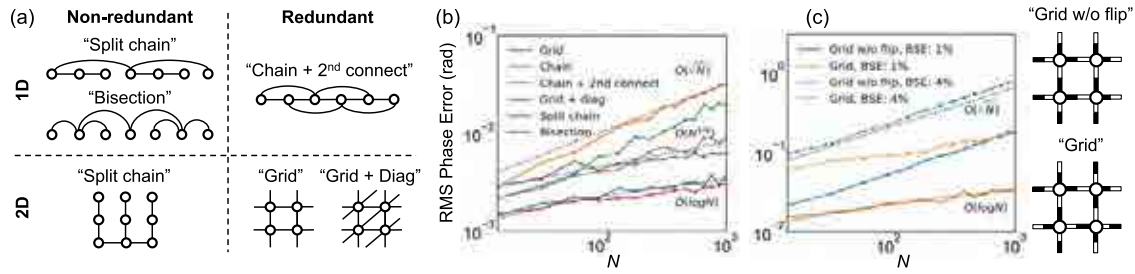
Fig. 5. (a) Configurations categorized into 1D, 2D, non-redundant, and redundant. (b) RMS phase sensing error with respect to the number of input ports N when photodetection noise is present (SNR = 30 dB). Designs following the design rule (e.g., "split chain," "grid") achieve better scalability compared to the naive chain configuration. (c) Impact of phase sensor polarity selection with biased error. Grid configuration achieves better scalability by flipping the edge polarities in "Grid w/o flip" configuration.
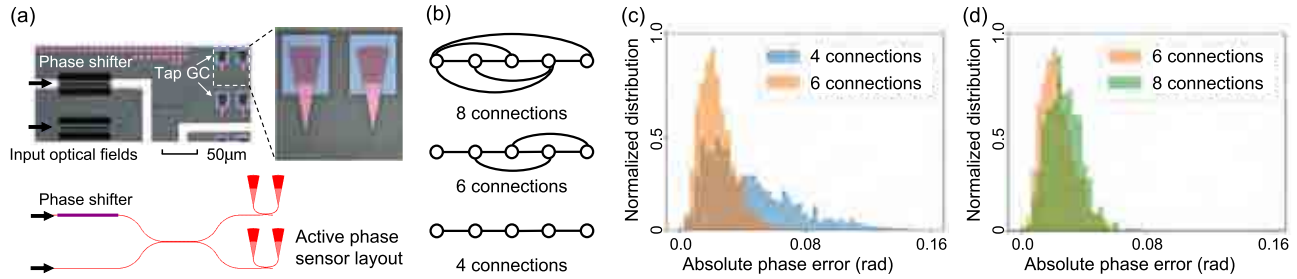

Fig. 6. Experimental demonstration of redundant phase sensor array with five input ports. (a) A single fabricated active phase sensor on silicon PIC with thermal phase shifter and tap grating coupler (tap GC) [12]. The measurement circuit consists of multiple phase sensors, as shown in Supplement 1 Fig. 3. (b) Non-redundant circuit configuration with four phase sensors and redundant configuration with six phase sensors. (c), (d) Absolute phase sensing error distributions over 1000 experiments with random input light field. Six connection configuration reduces error by ∼2× compared to non-redundant four connection configuration, while eight connection configuration leads to slightly worse accuracy due to the trade-off between system redundancy and per-sensor SNR with a small number of ports.

phase sensors [Fig. 6(b) lower], while the redundant phase sensor array utilizes six phase sensors [Fig. 6(b) middle]. We generate 1000 random input light fields following Eq. (5) and measure the phase profile following Eq. (4). Despite the optical power in each phase sensor being lower, the redundancy reduces the average phase sensing error by ∼2×. As shown in Fig. 6(c), the redundant circuit design is beneficial in this proof-of-concept demonstration, consistent with the simulation results discussed in Section 5.B. As the PIC scales, the benefit from the redundant circuit configuration is expected to be more significant.

Note that an excessive amount of redundancy can also be unfavorable. As shown in Figs. 6(b) and 6(d), we tested another configuration with eight connections [more redundant relative phase measurements, Fig. 6(b) upper]. However, the eight connection configuration achieves slightly worse accuracy compared to the six connection configuration. This is due to the trade-off between system redundancy and per-sensor SNR. With excessive redundancies, the input optical power is too distributed and SNR in each phase sensor is low. With a small number of input ports, this effect overwhelms the benefit from robustness in the phase profile estimation process, thus leading to less favorable performance.

In Fig. 7, we further demonstrate measuring the phase profile of free-space incident light with the PIC phase sensor array. We shine a plane wave onto three input ports (two phase sensors) and use a gimbal to control the angle of the incident beam. We use a fiber array to couple light off the chip and measure the optical power with off-chip photodetectors to avoid stray lights from the incident beam. As shown in Fig. 7(b), our system achieves a good linear relationship between the relative phase measurements

and the beam incident angle, especially after averaging to remove distortions induced by hardware errors. Considering the errors in manually tuning the gimbal rotation, our result demonstrates the accuracy and stability of the proposed reference-free phase sensors when measuring the free-space light field.

6. APPLICATIONS

Here we show two example applications of the proposed phase sensor array with simulated photonics circuits with larger scales.

A. Application 1: Phase Imaging

The most natural application of the phase sensor array is in microscopic phase imaging. Phase unwrapping is an important technique that solves the 2π phase ambiguity in the measured phase (wrapped between $[0, 2\pi]$). In an ideal system without measurement errors (noise), this process can be accurately resolved based on simple differentiation. However, small errors in the raw measurements are exaggerated in the unwrapping process [47,48]. As an example, we simulate a 128×128 resolution scene in Fig. 8(a), with SNR = 20 dB. Both the 2D "split chain" sensor array and the 2D grid sensor array achieve close to the ground truth wrapped phase image. We use a phase unwrapping library based on the noncontinuous path algorithm [49]. The small errors in the 2D "split chain" measurement result leads to large deviations from ground truth in the unwrapped phase images. On the other hand, the phase measurement of the redundant 2D grid design remains robust in the unwrapping process.
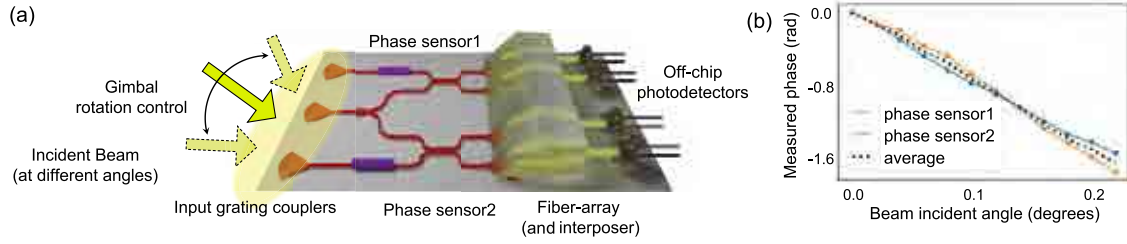
Fig. 7. (a) Free space phase sensing setup: experimentally measuring the phase of an incident plane wave at three input ports (two phase sensors). We use a gimbal to control incident angle of the beam. (b) Our setup presents a good linear relationship between the relative phase measurement and the beam incident angle.
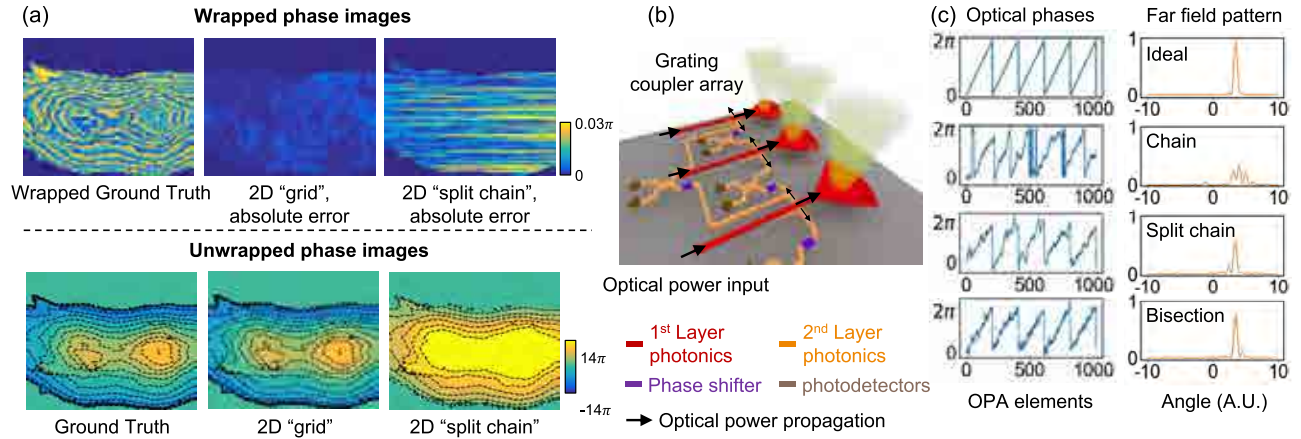

Fig. 8. (a) Comparisons on 128×128 resolution phase imaging and unwrapping with photodetection noise. The redundant 2D grid sensor array achieves more robust performance. (b) Schematic showing the application of proposed phase sensor array in optical phased array (OPA) phase monitoring. A dual-layer photonics circuit is used for simpler routing. Small amount of power is tapped out from the first layer into the second layer for phase monitoring. We use black arrows to visualize the optical power propagation. (c) Optical phase profile and far field pattern in $N = 1024$ 1D OPA, with "chain," "split chain," and "bisection" phase sensor arrays for phase monitoring. With better phase monitoring design, phase error is significantly reduced and far field pattern has better sidelobe suppression.

B. Application 2: On-Chip Phase Monitoring

Apart from measuring the optical phase of a free-space light field, the proposed system can also be applied in on-chip phase monitoring. Here we show one simulated example in an OPA [30]. OPAs are widely applied in communication [10,11], remote sensing [3–5], and augmented reality [50]. An OPA consists of multiple light-emitting antennas, and by adjusting the phase and amplitude in each antenna, an optical power distribution (pattern) is projected to the far field. Accurate phase monitoring is required to generate the desired far field pattern. We show an example in Fig. 8(b). The phase monitoring is here proposed to be implemented with a dual-layer photonics circuit [51] for simpler waveguide routing. A small amount of power is tapped out from the first layer into the second layer for phase monitoring, and we use black arrows to visualize the optical power propagation. Previously, chain configuration phase sensor arrays have been demonstrated for this application, in a relatively small OPA [52,53]. When the number of antenna elements increases, error accumulation becomes more significant. We simulate a 1D OPA with $N = 1024$ antennas. We assume low $\text{SNR} = 7$ dB in each phase sensor, since only a small amount of optical power is tapped out for phase monitoring to keep the optical efficiency of OPA high. As shown in Fig. 8(c), with more robust phase sensor array configurations ("split chain," "bisection"), both the phase profile and far field patterns have significantly higher quality compared to the naive chain configuration.

Table 1.   Summary of Metrics[a]

	Progressive [27]	**Phase Sensor Array**
Redundant	No	Yes
Time complexity	$8t_0 + 5t_1 \log N$	$2(t_0 + t_1)$ or t_0
Scalability	$O(\log N)$	$O(\log N)$
Computational cost	$O(N)$	$O(N^2)$
Electronics complexity	DAC required	Digital only or passive

[a]Red color indicates worse; green color indicates better.

7. DISCUSSION

Here we perform a similar phase sensing accuracy analysis on the progressive self-configuration approach [27] (most relevant prior art) and summarize the comparisons with the proposed approach in Fig. 9 and Table 1. A schematic of the architecture used in the progressive approach is shown in Fig. 9(a). The circuit consists of $\log N$ layers of MZIs, each containing two tunable phase shifters and two 50/50 beam splitters.

We suppose the photodetector exposure time is set to t_0 to achieve a specific SNR, and the phase shifter tuning time is t_1 due to the electronic/thermal bandwidth limit. The proposed low-latency phase sensor requires $2(t_0 + t_1)$ (active) or t_0 (passive) measurement time. In the progressive approach, the phase measurement process is conducted by nullifying optical powers in each circuit layer progressively [27]. A single nullification process can be implemented with a phase shifter sweeping + local
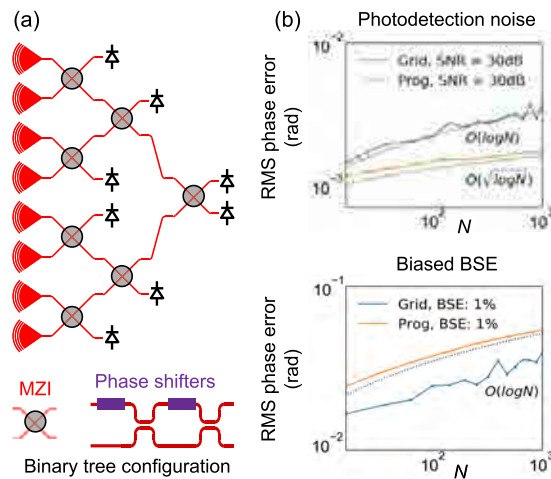
Fig. 9. Comparison between progressive approach [27] and proposed phase sensor array approach. (a) Schematic showing the photonics circuit of the progressive phase measurement approach [27] with a binary tree architecture. (b) Scalability comparisons between progressive and proposed phase sensor array (grid configuration).

feedback control [54]. Although this process is able to generate accurate measurement results, it involves at least tens or hundreds of phase shifter tuning and photodetector exposure periods. To make a fair comparison, we use five measurement steps for each nullification process. Also, since optical power accumulates after each nullification step, the exposure time used in the next layer can be reduced accordingly (we assume the exposure time can be arbitrarily short for simplicity. This results in a total time complexity $\sim 2t_0 + 5t_1 \log N$. When t_1 is longer than or comparable to t_0 (which is typical in current systems), this is a considerable increase in latency compared to the proposed phase sensor array.

Other important metrics include computational cost and electronics complexity. Since the progressive approach relies on tunable MZIs, it is hard to reduce the form factor, especially for tunable phase shifters, as discussed in Section 2. Also, analog control of the phase shift with high enough precision is required. On the other hand, the proposed phase sensor array can be either totally passive or have a binary phase shifter control (switching between zero and $\pi/2$). The progressive approach requires one optical field backpropagation simulation, which takes $O(N)$ computational cost, while the proposed phase sensor array requires one matrix–vector multiplication, which takes $O(N^2)$ computational cost. This is a comparatively minor drawback since computation in the digital domain is comparatively cheaper.

As shown in Fig. 9(b), when only photodetector noise is present, scalability of the progressive approach can achieve $O(\sqrt{\log N})$, better than the designed configurations. With biased hardware error, the scalability is comparable to the proposed phase array [both $O(\log N)$] but with a slightly higher coefficient. The good scalability of the progressive approach is due to the short error accumulation path length in the binary tree architecture (similar to the "bisection" configuration in Fig. 5), and to the optical power accumulation in the progressive programming process. Concentrated optical power leads to high SNR and low phase sensing errors in each element. We discuss applying the low-latency, passive phase sensors in such binary tree architecture in more detail in Supplement 1: although the path length remains short, without progressive optical power accumulation, such a system does not possess satisfying accuracy or scalability.

Apart from the hardware error and measurement noise analysis, there is another advantage of having redundant elements in the phase sensor array. As an example, suppose the right-most MZI node in Fig. 9(a) is malfunctioning; the entire measurement fails, while there is no method to easily tell which part of the circuit is causing the error. However, a redundant phase sensor array (as proposed in Fig. 5) is not influenced by a few malfunctioning/broken elements. Also, from the least squares solving process [Eq. (4)], it is easy to distinguish malfunctioning elements with the residual error. We show in Supplement 1 that such a system is still robust with >10% malfunctioning/broken elements.

8. CONCLUSION

Fast and simple optical phase measurement is important in optical communication and sensing. In this paper, we propose a low-latency, reference-free optical phase sensor based on integrated photonics. We demonstrate post-processing algorithms and circuit design rules (e.g., connection path length, redundancies, and polarities of phase sensor elements) that enable high accuracy and scalability in the presence of measurement noise and hardware errors. This leads to improved accuracy and robustness in applications across disciplines, including microscopy, remote sensing, optical computing, and optical communication.

REFERENCES

1. G. Popescu, *Quantitative Phase Imaging of Cells and Tissues* (McGraw-Hill Education, 2011).
2. Y. Park, C. Depeursinge, and G. Popescu, "Quantitative phase imaging in biomedicine," Nat. Photonics **12**, 578–589 (2018).
3. C. Rogers, A. Y. Piggott, D. J. Thomson, R. F. Wiser, I. E. Opris, S. A. Fortune, A. J. Compston, A. Gondarenko, F. Meng, X. Chen, G. T. Reed, and R. Nicolaescu, "A universal 3D imaging sensor on a silicon photonics platform," Nature **590**, 256–261 (2021).
4. C. V. Poulton, A. Yaacobi, D. B. Cole, M. J. Byrd, M. Raval, D. Vermeulen, and M. R. Watts, "Coherent solid-state lidar with silicon photonic optical phased arrays," Opt. Lett. **42**, 4091–4094 (2017).
5. Y. Wang, G. Zhou, X. Zhang, K. Kwon, P.-A. Blanche, N. Triesault, K.-S. Yu, and M. C. Wu, "2D broadband beamsteering with large-scale mems optical phased array," Optica **6**, 557–562 (2019).
6. Z. Zhan, M. Cantono, V. Kamalov, A. Mecozzi, R. Müller, S. Yin, and J. C. Castellanos, "Optical polarization–based seismic and water wave sensing on transoceanic cables," Science **371**, 931–936 (2021).
7. A. Mecozzi, M. Cantono, J. C. Castellanos, V. Kamalov, R. Muller, and Z. Zhan, "Polarization sensing using submarine optical cables," Optica **8**, 788–795 (2021).
8. D. A. Miller, "Establishing optimal wave communication channels automatically," J. Lightwave Technol. **31**, 3987–3994 (2013).
9. K. Choutagunta, I. Roberts, D. A. Miller, and J. M. Kahn, "Adapting Mach–Zehnder mesh equalizers in direct-detection mode-division-multiplexed links," J. Lightwave Technol. **38**, 723–735 (2019).
10. C. V. Poulton, M. J. Byrd, P. Russo, E. Timurdogan, M. Khandaker, D. Vermeulen, and M. R. Watts, "Long-range lidar and free-space data communication with high-performance optical phased arrays," IEEE J. Sel. Top. Quantum Electron. **25**, 7700108 (2019).

11. J. He, T. Dong, and Y. Xu, "Review of photonic integrated optical phased arrays for space optical communication," IEEE Access **8**, 188284 (2020).

12. S. Pai, Z. Sun, T. W. Hughes, T. Park, B. Bartlett, I. A. Williamson, M. Minkov, M. Milanizadeh, N. Abebe, F. Morichetti, A. Melloni, S. Fan, O. Solgaard, and D. A. B. Miller, "Experimentally realized in situ backpropagation for deep learning in photonic neural networks," Science **380**, 398–404 (2023).

13. S. Pai, B. Bartlett, O. Solgaard, and D. A. Miller, "Matrix optimization on universal unitary photonic devices," Phys. Rev. Appl. **11**, 064044 (2019).

14. I. A. Williamson, T. W. Hughes, M. Minkov, B. Bartlett, S. Pai, and S. Fan, "Reprogrammable electro-optic nonlinear activation functions for optical neural networks," IEEE J. Sel. Top. Quantum Electron. **26**, 7700412 (2019).

15. Y. Shen, N. C. Harris, S. Skirlo, M. Prabhu, T. Baehr-Jones, M. Hochberg, X. Sun, S. Zhao, H. Larochelle, D. Englund, and M. Soljačić, "Deep learning with coherent nanophotonic circuits," Nat. Photonics **11**, 441–446 (2017).

16. B. L. Schumaker, "Noise in homodyne detection," Opt. Lett. **9**, 189–191 (1984).

17. E. Ip, A. P. T. Lau, D. J. Barros, and J. M. Kahn, "Coherent detection in optical fiber systems," Opt. Express **16**, 753–791 (2008).

18. W. Hou and G. Wilkening, "Investigation and compensation of the nonlinearity of heterodyne interferometers," Precis. Eng. **14**, 91–98 (1992).

19. T. Eom, T. Choi, K. Lee, H. Choi, and S. Lee, "A simple method for the compensation of the nonlinearity in the heterodyne interferometer," Meas. Sci. Technol. **13**, 222 (2002).

20. C. J. Karlsson and F. Å. Olsson, "Linearization of the frequency sweep of a frequency-modulated continuous-wave semiconductor laser radar and the resulting ranging performance," Appl. Opt. **38**, 3376–3386 (1999).

21. S. M. Popoff, G. Lerosey, R. Carminati, M. Fink, A. C. Boccara, and S. Gigan, "Measuring the transmission matrix in optics: an approach to the study and control of light propagation in disordered media," Phys. Rev. Lett. **104**, 100601 (2010).

22. A. Drémeau, A. Liutkus, D. Martina, O. Katz, C. Schülke, F. Krzakala, S. Gigan, and L. Daudet, "Reference-less measurement of the transmission matrix of a highly scattering material using a DMD and phase retrieval techniques," Opt. Express **23**, 11898–11911 (2015).

23. Y. Wu, M. K. Sharma, and A. Veeraraghavan, "Wish: wavefront imaging sensor with high resolution," Light Sci. Appl. **8**, 1–10 (2019).

24. B.-Y. Wang, L. Han, Y. Yang, Q.-Y. Yue, and C.-S. Guo, "Wavefront sensing based on a spatial light modulator and incremental binary random sampling," Opt. Lett. **42**, 603–606 (2017).

25. C. Wang, X. Dun, Q. Fu, and W. Heidrich, "Ultra-high resolution coded wavefront sensor," Opt. Express **25**, 13736–13746 (2017).

26. B. C. Platt and R. Shack, "History and principles of Shack-Hartmann wavefront sensing," J. Refract. Surg. **17**, S573–S577 (2013).

27. D. A. Miller, "Analyzing and generating multimode optical fields using self-configuring networks," Optica **7**, 794–801 (2020).

28. J. Bütow, J. S. Eismann, M. Milanizadeh, F. Morichetti, A. Melloni, D. A. Miller, and P. Banzer, "Spatially resolving amplitude and phase of light with a reconfigurable photonic integrated circuit," Optica **9**, 939–946 (2022).

29. A. Khachaturian, R. Fatemi, and A. Hajimiri, "Iq photonic receiver for coherent imaging with a scalable aperture," IEEE Open J. Solid-State Circuits Soc. **1**, 263–270 (2021).

30. P. F. McManamon, T. A. Dorschner, D. L. Corkum, L. J. Friedman, D. S. Hobbs, M. Holz, S. Liberman, H. Q. Nguyen, D. P. Resler, R. C. Sharp, and E. A. Watson, "Optical phased array technology," Proc. IEEE **84**, 268–298 (1996).

31. R. Diestel, A. Schrijver, and P. Seymour, "Graph theory," Oberwolfach Rep. **4**, 887–944 (2008).

32. D. Taillaert, P. Bienstman, and R. Baets, "Compact efficient broadband grating coupler for silicon-on-insulator waveguides," Opt. Lett. **29**, 2749–2751 (2004).

33. A. Mekis, S. Gloeckner, G. Masini, A. Narasimha, S. Pinguet, S. Sahni, and P. De Dobbelaere, "A grating-coupler-enabled CMOS photonics platform," IEEE J. Sel. Top. Quantum Electron. **17**, 597–608 (2010).

34. S. G. Leon-Saval, A. Argyros, and J. Bland-Hawthorn, "Photonic lanterns," Nanophotonics **2**, 429–440 (2013).

35. M. Zhang, R. Malureanu, A. C. Krüger, and M. Kristensen, "1x3 beam splitter for te polarization based on self-imaging phenomena in photonic crystal waveguides," Opt. Express **18**, 14944–14949 (2010).

36. G. C. Holst, *CMOS/CCD Sensors and Camera Systems* (2007).

37. S. Boyd and L. Vandenberghe, *Introduction to Applied Linear Algebra: Vectors, Matrices, and Least Squares* (Cambridge University, 2018).

38. S. W. Hasinoff, *Photon, Poisson Noise* (2014).

39. M. Piels and J. E. Bowers, "Photodetectors for silicon photonic integrated circuits," in *Photodetectors* (2016), pp. 3–20.

40. H. Chen, P. Verheyen, P. De Heyn, G. Lepage, J. De Coster, S. Balakrishnan, P. Absil, G. Roelkens, and J. Van Campenhout, "Dark current analysis in high-speed germanium pin waveguide photodetectors," J. Appl. Phys. **119**, 213105 (2016).

41. F. Hooge, T. Kleinpenning, and L. K. Vandamme, "Experimental studies on 1/f noise," Rep. Prog. Phys. **44**, 479 (1981).

42. S. Bandyopadhyay, R. Hamerly, and D. Englund, "Hardware error correction for programmable photonics," Optica **8**, 1247–1255 (2021).

43. D. A. Miller, "Perfect optics with imperfect components," Optica **2**, 747–750 (2015).

44. T.-W. Weng, Z. Zhang, Z. Su, Y. Marzouk, A. Melloni, and L. Daniel, "Uncertainty quantification of silicon photonic devices with correlated and non-Gaussian random parameters," Opt. Express **23**, 4242–4254 (2015).

45. Z. Lu, J. Jhoja, J. Klein, X. Wang, A. Liu, J. Flueckiger, J. Pond, and L. Chrostowski, "Performance prediction for silicon photonics integrated circuits with layout-dependent correlated manufacturing variability," Opt. Express **25**, 9712–9733 (2017).

46. F. R. Chung, *Spectral Graph Theory* (American Mathematical Soc., 1997), Vol. **92**.

47. W. Zhu and G. C. Beroza, "Phasenet: a deep-neural-network-based seismic arrival-time picking method," Geophys. J. Int. **216**, 261–273 (2019).

48. G. Spoorthi, R. K. S. S. Gorthi, and S. Gorthi, "Phasenet 2.0: phase unwrapping of noisy data based on deep learning approach," IEEE Trans. Image Process. **29**, 4862–4872 (2020).

49. M. A. Herráez, D. R. Burton, M. J. Lalor, and M. A. Gdeisat, "Fast two-dimensional phase-unwrapping algorithm based on sorting by reliability following a noncontinuous path," Appl. Opt. **41**, 7437–7444 (2002).

50. J. Notaros, M. Raval, M. Notaros, and M. R. Watts, "Integrated-phased-array-based visible-light near-eye holographic projector," in *Conference on Lasers and Electro-Optics (CLEO)* (IEEE, 2019), pp. 1–2.

51. P. Wang, G. Luo, Y. Xu, Y. Li, Y. Su, J. Ma, R. Wang, Z. Yang, X. Zhou, Y. Zhang, and J. Pan, "Design and fabrication of a SiN-Si dual-layer optical phased array chip," Photonics Res. **8**, 912–919 (2020).

52. A. R. Alves Júnior, K. Miura, T. Spuesens, and W. Bogaerts, "Phase shift control with active feedback," in *Proceedings Symposium IEEE Photonics Society Benelux* (2016), pp. 291–294.

53. J. Shim, J.-B. You, H.-W. Rhee, H. Yoon, S.-H. Kim, K. Yu, and H.-H. Park, "On-chip monitoring of far-field patterns using a planar diffractor in a silicon-based optical phased array," Opt. Lett. **45**, 6058–6061 (2020).

54. A. Ribeiro, A. Ruocco, L. Vanacker, and W. Bogaerts, "Demonstration of a 4× 4-port universal linear circuit," Optica **3**, 1348–1357 (2016).

55. S. Pai and T. Park, "phox: repository for simulation and control of photonic devices," GitHub, 2023, https://github.com/solgaardlab/phox.